Seasonal variations of Mg and Ca in the exosphere of Mercury

Jean-yves Chaufray, François Leblanc, Elisabeth Werner, Ronan Modolo, S. Aizawa

Seasonal variations of Mg and Ca in the exosphere of Mercury

J-Y. Chaufray[1], F. Leblanc[1], A.I.E. Werner[1], R. Modolo[1], S. Aizawa[2]

[1]LATMOS-IPSL, CNRS, Sorbonne-Université, Paris-Saclay, Paris, France

[2]IRAP, CNRS, Toulouse, France

Abstract

We simulate the seasonal variations of the Mg 285.3 nm and Ca 422.7 nm brightness and compared our results to the MESSENGER/MASCS observations at dawn. Our results are consistent with the previous studies of Ca while for Mg we used another seasonal variation for the g -value (excitation frequency) at 285.3 nm. We find that both emissions are well reproduced from micrometeoroid impacts when the true anomaly angle (TAA) of Mercury is larger than 80°. For true anomaly angle lower than 80°, an additional source is needed to reproduce the Ca observations in agreement with previous studies, and possibly the Mg observations. We compare several solar spectra (observed or modeled) to study the Mg g-value and found that the seasonal variation of the g-value peaking near TAA=60° used by previous studies to analyse the MESSENGER observations of Mg may be due to an artefact not present in the solar spectrum. The observed seasonal variations of the Mg brightness are better reproduced without this artefact. However, observations of the solar spectrum near 285.3 nm at a spectral resolution of ~ 20 mA would be needed to better estimate the seasonal variations of the Mg excitation frequencies and then to better understand the possible differences in the source of these two species in the exosphere of Mercury.

1) Introduction

As the Moon, Mercury does not have an atmosphere but only a very tenuous surface-bounded exosphere (Stern 1999). This exosphere was observed for the first time during the three flybys of Mercury by the NASA mission Mariner 10 in 1974 and 1975 (Broadfoot et al. 1976) and later from ground-based observations during more than 30 years (Potter and Morgan 1985, see the reviews by Leblanc et al. 2007 and Killen et al. 2007). Calcium was observed only sporadically from ground-based observations (Bida et al. 2000, Killen et al. 2005). The study of these sporadic Ca observations indicated a very tenuous and hot population (T ~ 12,000K) much hotter than the Mercury's surface temperature. After three flybys of Mercury, during which, among other things, magnesium was detected for the first time by the Mercury Atmospheric and Surface Composition Spectrometer / Ultraviolet and Visible Spectrometer (MASCS/UVVS) (McClintock and Lankton, 2007, McClintock et al., 2008, 2009), MESSENGER was the first mission inserted in orbit around Mercury from March 2011 to April 2015. During this orbital phase, Na, Ca and Mg were regularly observed allowing a detailed study of their temporal (seasonal, diurnal) variations. A detailed summary of these observations can be found in the review paper by McClintock et al. (2018) and a broader context comparing observations of Mercury and the Moon can be found in Leblanc et al. (2021) and Grava et al. (2021).

The observations of the Ca emissions during the orbital phase were studied by Burger et al. (2012, 2014). The authors derive a large temperature (~70,000K) fromthe vertical profile of the observed brightness. This temperature is several times larger than the temperature derived from linewidth that had been derived from ground observations (Bida et al. 2000, Killen et al. 2005). This large temperature excluded numerous sources and favored a meteoroids impact

52 vaporization (MIV) source for Ca bearing molecules, followed by their photodissociation, in
53 the exosphere of Mercury (Killen 2016).

54 Burger et al. (2012, 2014) also found a large dawn/dusk asymmetry and were able to derive the
55 source rate needed to reproduce the variations along one Mercury year, while no year to year
56 variations was observed. Killen and Hahn (2015) presented a dust model to reproduce the
57 seasonal variations of the source rate derived by Burger et al. (2014). This model includes dust
58 coming from an interplanetary dust disk with an additional source near Mercury's true anomaly
59 angle $\nu = 25\pm5°$ attributed to 2P/Encke comet stream (Christou et al. 2015). A more
60 sophisticated model of interplanetary dust disk was also proposed by Pokorny et al. (2018) who
61 also study its local time variations and show a flux nearly peaking at dawn, and minimum near
62 dusk all along the Mercury year and confirmed that another source was needed to reproduce the
63 source rate near $\nu = 25°$.

64 The observations of Mg were studied by Merkel et al. (2017, 2018) who found a dawn/dusk
65 asymmetry of the brightness with a maximum at dawn and a minimum at dusk quite similar to
66 Ca. While the interpretation of the observations done during the flybys suggested two
67 populations (Sarantos et al. 2011) : one at low energy (< 5000K) and one at high energy (>
68 20,000K), Merkel et al. (2017) only needed one population (T~ 6000K) to reproduce most of
69 the vertical profiles observed during the MESSENGER orbital phase with evidence for two
70 temperature distribution near dawn terminator for 15% of the time. A temperature of 6000 K is
71 consistent with the photodissociation of Mg-bearing molecules or oxides produced from
72 impacts. Recently, Cassidy et al. (2021) report transient events in Mercury nightside tail. They
73 suggest cm-sized impactors producing a vapor temperature of ~ 10^4 K, larger than the average,
74 but in the range of temperatures derived by Merkel et al. (2017) to fit the Mg vertical profiles.
75 During one of the events, Na and Mg brightened simultaneously with a ratio consistent with
76 their surface abundance while no enhancement of Ca was observed. The lack of Ca

77 enhancement was consistent with Ca being bound in a molecule in the impact vapor not
78 photodissiociated because the impact was a nightside impact.

79 Merkel et al. (2017) also derived the seasonal variation of the source rate needed to reproduce
80 the observations from a Chamberlain's model (Chamberlain 1963). They found a peak source
81 near $\nu = 315°$ and no signature of an additional comet stream near $\nu = 25°$. While the seasonal
82 pattern has a year-to-year repeatability, a two-year cycle was reported by Merkel et al. (2018).
83 This biennial cycle results from the 3 :2 spin orbit of Mercury : the observed Mg brightness
84 being larger during the years when the region of Mercury's surface enriched in Mg (east
85 longitude ~270°; Weider et al. 2015) is at dawn than during the years when this region is at
86 dusk.

87 In this paper, we investigate the Ca and Mg MESSENGER/MASCS observations of the orbital
88 phase from several Mercury's years, using a 3D exospheric model of Mercury to check if the
89 dust sources proposed to explain the Ca observations by Killen and Hahn (2015) can also
90 explain fully, partly or not the Mg observations. In Section 2, we introduce the data set used in
91 our study. Our exospheric model and the assumptions used to describe Ca and Mg in the
92 exosphere of Mercury are presented in Section 3. The simulation results and comparison with
93 MESSENGER/MASCS observations are presented in Section 4 and discussed in Section 5,
94 followed by a conclusion in Section 6.

95

96 **2) MESSENGER/MASCS Observations**

97 MESSENGER was inserted into a highly eccentric 12-h orbit around Mercury on 18 March
98 2011. The initial orbit had an inclination of 82.5°, an apoapsis of 15,200 km in the southern
99 hemisphere and a periapsis of 200 km in the northern hemisphere. The periapsis altitude varied
100 between 200 – 500 km during the primary mission due to gravitational perturbations of the

spacecraft trajectory (Solomon et al. 2018). During the first extension (March 2012) the period of the orbit was reduced to 8-h and the apoapsis decreased to 10,300 km (Solomon et al. 2018).

During the second extension (from 18 March 2013 to 18 March 2015), the periapsis altitude was lowered from 450 km down to the surface on 30 April 2015. Regular campaigns of observations of the exosphere were performed during these two extensions by MASCS-UVVS. Most of the observations were performed near the apoapsis. In this paper, we consider one of the primary sequence of observations executed by UVVS. It corresponds to dayside limb scans performed at different local times, used to study the altitude, local time and seasonal variations of the exospheric emissions (McClintock et al. 2018). We only consider the profile measured near 6 am local time from Mercury year 5 to Mercury year 17 (The Mercury Year 1 corresponds to the orbital insertion of MESSENGER). The geometry of the observation at 6 am, during the MESSENGER orbit #2507, on Mercury Year 11 is displayed in Fig. 1

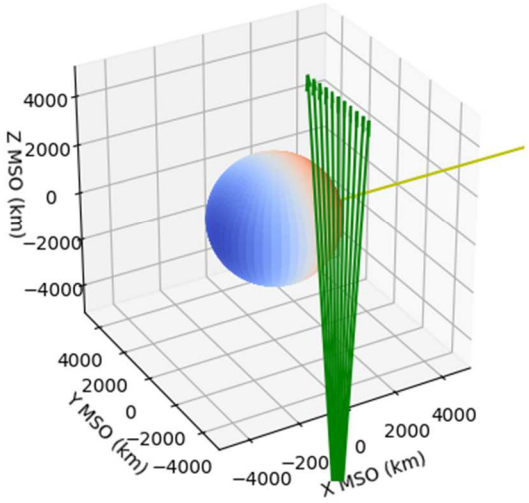

Fig. 1 Geometry of one observation performed when MESSENGER was close to its apoapsis during orbit #2507 (Mercury year 11) in Mercury Solar Orbital (MSO) frame. The lines of sight during the scan are shown in green. The Sun direction is indicated by the yellow line. The Mercury dayside surface is in light red and the nightside in blue.

The seasonal variations of the Ca and Mg brightness at tangent altitudes of 300 ±50 km including all the Mercury years are displayed in Fig. 2. The even and odd years are represented by different colors. For Mg, the brightness variations are similar to the variations presented by Merkel et al. (2017) with a maximum near perihelion and a minimum near aphelion. We can also notice the biennial cycle with a larger brightness after perihelion during odd years than during even years and the opposite before perihelion for Mg (A year is assumed to start at perihelion in this paper, contrary to the convention used by Merkel et al. 2018 in their Fig 1a, where the years are separated at aphelion). The seasonal variations of the Ca emissions are similar to the Mg seasonal variations, but without a detectable biennial cycle in agreement with Burger et al. (2014).

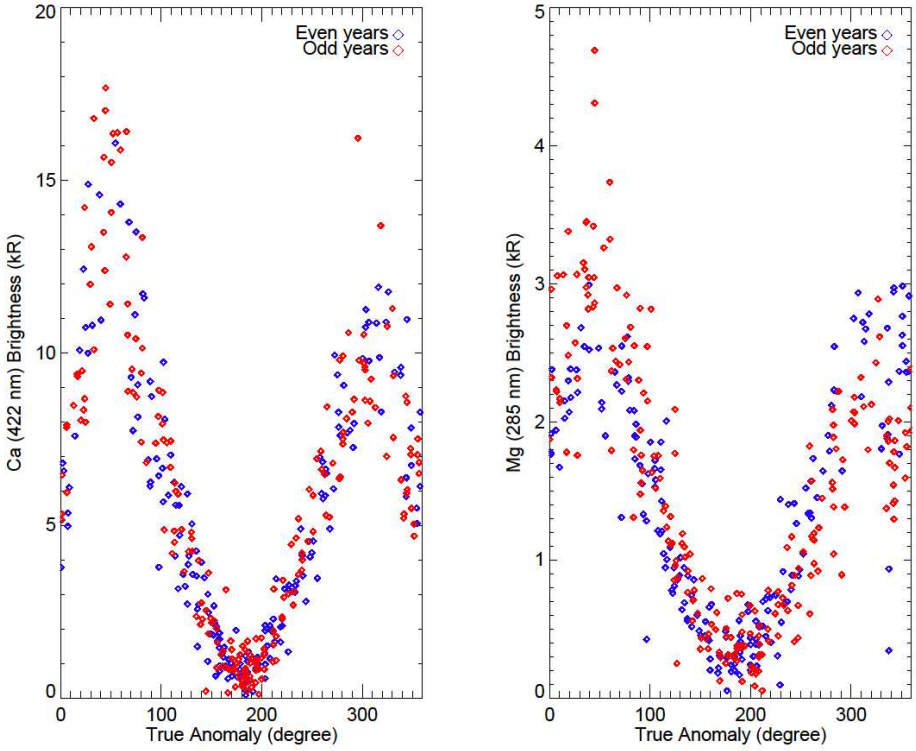

Fig. 2 Left : Seasonal variations of the calcium emission near 6 am at 300 km, derived from Mercury years 7 to 17 from MESSENGER/MASCS-UVVS. Right: Seasonal variations of the magnesium emission near 6 am at 300 km, derived from Mercury years 7 to 17 from MESSENGER/MASCS-UVVS.

3) Exospheric model

3.1) EGM

The LATMOS Exospheric Global Model (EGM) has been developed to simulated the 3D exospheric density of several objects in the solar system, including for example : oxygen on Mars (Leblanc et al. 2017), sodium on Mercury (Leblanc et al. 2013), oxygen and water on Ganymede and Europa (Leblanc et al. 2017, Oza et al. 2019). EGM is a 3D, time-dependent, spherical Monte Carlo model solving the Boltzmann (or Liouville) equation to compute the exospheric density, and other moments of the velocity distribution functions. For Mercury, this model includes the revolution of Mercury around the Sun and the rotation of Mercury. The exosphere of Mercury is divided in several cells from the surface to 4 Mercury radii (~ 10,000 km). The space is described by spherical coordinates in Mercury-Solar Orbital (MSO) frame. The radial axis is divided into 80 cells with a vertical resolution varying from 5 km near the surface to 300 km near the upper boundary. The latitudinal axis is divided into 20 cells with a resolution varying from ~6° at the equator to ~25° near the poles. The zonal axis is divided into 40 cells with a uniform angular size of 9°.

We assume all the calcium and magnesium atoms in the exosphere of Mercury to be ejected after interplanetary dust impact on the surface of Mercury. Other possible sources (sputtering, photon desorption, thermal desorption) are neglected following the conclusions of Burger et al. (2012, 2014) and Merkel et al. (2017, 2018). For Mg, the local ejection rate is proportional to the local dust impact flux and the local Mg/Si ratio at the surface, while we consider a constant value for Ca/Si. In each exospheric cell near the surface, a constant number of test particles is ejected regularly. The variation of the ejection rate is taken into account through the weight of the test-particle (i.e. the number of real atoms represented by one test particle) defined by

$$W = A \times F_{dust}(\varphi, \theta, \nu) \times n_s(\alpha, \beta) \times S_{cell} \times \Delta t \quad (1)$$

where $F_{dust}(\varphi,\theta,\nu)$ is the dust impact flux at MSO longitude φ and co-latitude θ and true anomaly angle ν, S_{cell} is the surface of the cell, Δt the period of ejection in the simulation and $n_s(\alpha,\beta)$ the

surface ratio of Mg/Si at planetary longitude α and latitude β, assuming a uniform Si concentration at the surface and a constant value for Ca/Si (see Section 3.3). These two terms are detailed in Section 3.2. *A* is a free parameter fitted from MESSENGER Ca observations..

The test particles are then followed along their trajectory until they are lost from the simulation. In our simulations, Ca and Mg test particles can be lost by three processes :

Impact onto the surface : In all our simulations, we assume that any Mg or Ca test particle that impacts the surface is trapped and lost for the exosphere. This is the dominant loss process for Mg.

Escape : A test particle is considered to be lost if it reaches the upper boundary of the model, whatever its velocity. In fact, if we neglect the radiation pressure, only particles with a velocity larger than the escape velocity should be lost, but the fraction of particles reaching the upper boundary with a velocity lower than the escape velocity is a minor fraction of the lost particles for Ca and Mg.

Ionization : At each time step dt, a test particle located outside the Mercury's shadow has a probability $p = 1-\exp(-\nu_{ionization}dt)$ to be lost by photoionization, where $\nu_{ionization}$ is the photoionization frequency, which varies as $1/d^2$ where d is Mercury-Sun distance. For Mg, the ionization frequency is 4.4×10^{-7} s^{-1} at 1 AU and for Ca the ionization frequency is 6.6×10^{-5} s^{-1} at 1 AU close to the value used by Killen et al. (2018), see also the discussion in their Section 15.2.2.2. This is the dominant loss process for Ca.

The radiation pressure is included for both species. It is treated as a continuous force directed in the antisolar direction, without considering its stochastic character (Bzowski 1993). The effect of the radiation pressure on the exospheric density is different for Ca and Mg and is discussed in Section 4.

3.2) Dust flux model and surface density

To simulate the number of ejected Mg and Ca atoms from the surface, we use a model of interplanetary dust flux similar to Killen and Hahn (2015). In this model, the interplanetary dust is coming from three different populations : 1) Asteroids and the Jupiter family comets, 2) Halley type comets and 3) Oort cloud. Each population is characterized by an inclination distribution with respect to the dust disk midplane and a power law variation with the heliocentric distance. The inclination distribution of the two first populations are Gaussian while the distribution of the Oort clouds population is uniform. The parameters for each distribution, heliocentric power law, inclination for the mean dust disk plane, and its ascending node are taken from Killen and Hahn (2015) and the seasonal variation of the evaporation rate due to this mean dust disk is displayed in Fig. 3.. We also consider an additional dust flux peaking near $\nu_0 = 25°$, and with a seasonal Gaussian distribution, with $\sigma_\nu = 15°$ (Fig. 3) following the equation :

$$F_{Encke}(\nu) = F_{max} e^{-\frac{(\nu-\nu_0)^2}{2\sigma_\nu^2}} \quad (2)$$

This additional dust flux was attributed to the dust coming from Encke by Killen and Hahn (2015) and was needed to reproduce the Ca observations by MESSENGER.

There are some small differences between our seasonal variation of the evaporation rate compared with the variation calculated by Killen and Hahn (2015) (Fig. 3) that may result from the numerical integrations used to derive the dust density. We only consider relative variations along one Mercury's year, since the absolute values are tuned to fit the MESSENGER's observations through the free parameter A .

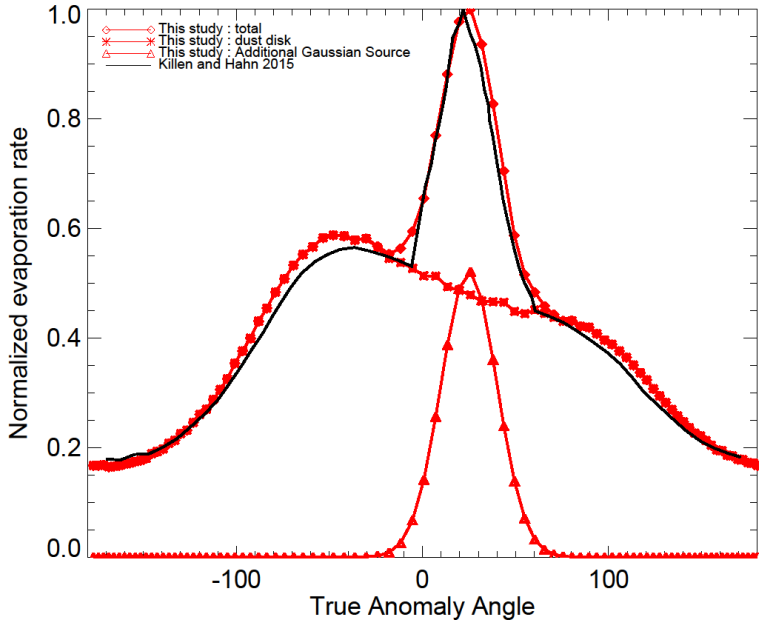

206

207 *Fig. 3 Variations of the impact vaporization rate induced by the mean dust disk and an*
208 *additional Gaussian source along Mercury's orbit simulated in EGM*

209 The dust impact flux at the surface of Mercury is not uniform (Pokorny et al. 2018). In our
210 simulation, we assume a distribution in Mercury Solar Orbital (MSO) coordinate system
211 independent on ν which is a relatively good assumption at first order compared to a more
212 sophisticated model (Pokorny et al. 2018) for the mean dust disk. We assume a similar
213 distribution for the additional Gaussian source. The impacting dust flux $F_{dust}(\varphi,\theta,\nu)$ is
214 decomposed as

215 $$F_{dust}(\varphi,\theta,\nu) = F(\nu)f(\varphi,\theta) \quad (3)$$

216 Where F(ν) is displayed in Fig. 3 and f(φ,θ) described the spatial distribution of the impacting
217 flux where φ is the MSO longitude and θ the MSO co-latitude. For f(φ, θ), we consider the
218 spatial distribution used by Burger et al. (2014) to fit the calcium observations by
219 MESSENGER defined by : $f(\varphi,\theta)=f_0 e^{-a\cos(\cos(\varphi+\pi/2)\sin(\theta))/\sigma}$, where σ = 0.87 rad (50°) is the angular
220 e-folding width of the source. The maximum of the impact flux is at dawn in the equatorial
221 plane θ = π/2, φ = 3π/2 and the minimum is at dusk in the equatorial plane θ =π/2, φ = π/2. The
222 f(φ, θ) distribution is simplified compared to the more sophisticated model of Pokorny et al.

223 (2018) which shows a slight nightside shift of the maxima (~ 4am) for a true anomaly $\nu < 180°$
224 and a slight dayside shift of the maxima (~ 8 am) for $\nu > 180°$. We consider that this more
225 precise description of this flux should not change our conclusion. Specific assumptions for each
226 species are presented below. All the ejected atoms are assumed to be in the electronic ground
227 state.

228

229 3.3) Calcium

230 The velocity distribution of the ejected calcium atoms is a Maxwellian-Boltzmann Flux (MBF)
231 distribution with a temperature of 70,000 K consistent with the value derived from the vertical
232 variations of the Ca intensity at 422 nm (Burger et al. 2014). This value is much larger than the
233 expected temperature due to dust impact from theoretical studies, but could be explained by a
234 shocked-induced dissociative ionization of Ca bearing molecules (Killen 2016). It corresponds
235 to an escape parameter $\lambda = 0.62$ at the surface.

236 Calcium could come from Mercury or from an extended dust cloud, in our simulation we will
237 assume that all Ca is coming from Mercury. MESSENGER/XRS produced maps of the surface
238 Ca/Si ratio showing variation between 0.05 and 0.30 but with uncomplete coverage of the
239 northern hemisphere due to MESSENGER orbit because Ca/Si is detected only during flares
240 (Weider et al. 2015). Therefore, in our simulations, we consider a uniform Ca/Si ratio = 0.15
241 and assume a surface density proportional to this ratio (i.e. assuming a constant Si surface
242 content). The absolute value of Si surface density is not needed for our modelling since it is
243 being included in the parameter A which is estimated to provide the best fit to the Ca
244 observations (Section 3.1).

245 3.4) Magnesium

246 For magnesium, we also consider a MBF distribution but a temperature of 6000K equal to the
247 average temperature derived from MESSENGER observations of Mg scale height (Merkel et

al. 2017). Contrary to calcium, we consider a non uniform distribution of the Mg/Si ratio at the surface, in order to reproduce the two year cycle observed by Merkel et al. (2018). The map of Mg/Si derived from MESSENGER/XRS has a global coverage because it can be observed during quiet and flare conditions (Weider et al. 2015) and is used as input to the model. The relation between the longitude in MSO frame φ at a given time t along Mercury's rotation and longitude in planetary frame α is derived by integration of the relative angular rotation :

$$\varphi(\alpha, t) = \varphi(\alpha, 0) + \frac{180}{\pi}\int_0^t (\omega_{rot} - \omega_{orb}(t'))dt' \quad (4)$$

Where, ω_{rot} is the sidereal angular velocity of Mercury and $\omega_{orb}(t')$ the time dependent orbital angular velocity, given by the Kepler's second law: $\omega_{orb}(t') = 2V_A/d^2(t')$, where V_A is the magnitude of the areal velocity, and d the Mercury-Sun distance. Replacing the integration over time t', by an integration over true anomaly ν, leads to

$$\alpha = [\varphi - \psi(\nu)] \quad (5a)$$

for Mercury odd years, and

$$\alpha = [\varphi - \psi(\nu) - 180] \quad (5b)$$

for Mercury even years

A Mercury year starts when Mercury is at its perihelion. At the beginning of an odd year, the subsolar point (φ =0°) is at longitude α =0° and at α = 180° at the beginning of an even year.

ψ(ν) is a function of the true anomaly angle derived analytically from direct integration of Eq. 4 (see appendix for details), and given by

$$\psi(\nu) = \frac{180}{\pi}\left(\frac{\omega_{rot}}{\langle\omega_{orb}\rangle}\sqrt{1-e^2}\left[\frac{2}{\sqrt{1-e^2}}tan^{-1}\left(\sqrt{\frac{1-e}{1+e}}\tan\left(\frac{\nu}{2}\right)\right) - \frac{esin\nu}{1+ecos\nu}\right] - \nu\right) \qquad \nu < \pi \quad (6a)$$

$$\psi(\nu) = \frac{180}{\pi}\left(\frac{\omega_{rot}}{\langle\omega_{orb}\rangle}\sqrt{1-e^2}\left[\frac{\pi}{\sqrt{1-e^2}} + \frac{2}{\sqrt{1-e^2}}tan^{-1}\left(\sqrt{\frac{1+e}{1-e}}\tan\left(\frac{\nu-\pi}{2}\right)\right) - \frac{esin\nu}{1+ecos\nu}\right] - \nu\right) \quad \nu>\pi \quad (6b)$$

Where e is Mercury orbital excentricity and $\langle\omega_{orb}\rangle$ the yearly average orbital angular velocity. For Mercury $\omega_{rot}/\langle\omega_{orb}\rangle = 3/2$.

4) Results

4.1) Calcium

4.1.1) Simulation results

We simulate several Mercury years. A periodic steady state is quickly reached during the first year (Fig. 4). Simulated seasonal variations of the Ca density are persistent and due to the variation of the dust impact flux, with a minimum near ν = 180° and a maximum at ν = 25°. Noise due to statistics in the Monte Carlo simulations is the source of the short time scale variations and of the year-to-year variations.

The density is always maximum at dawn and minimum at dusk, following the local time variations of the source term.

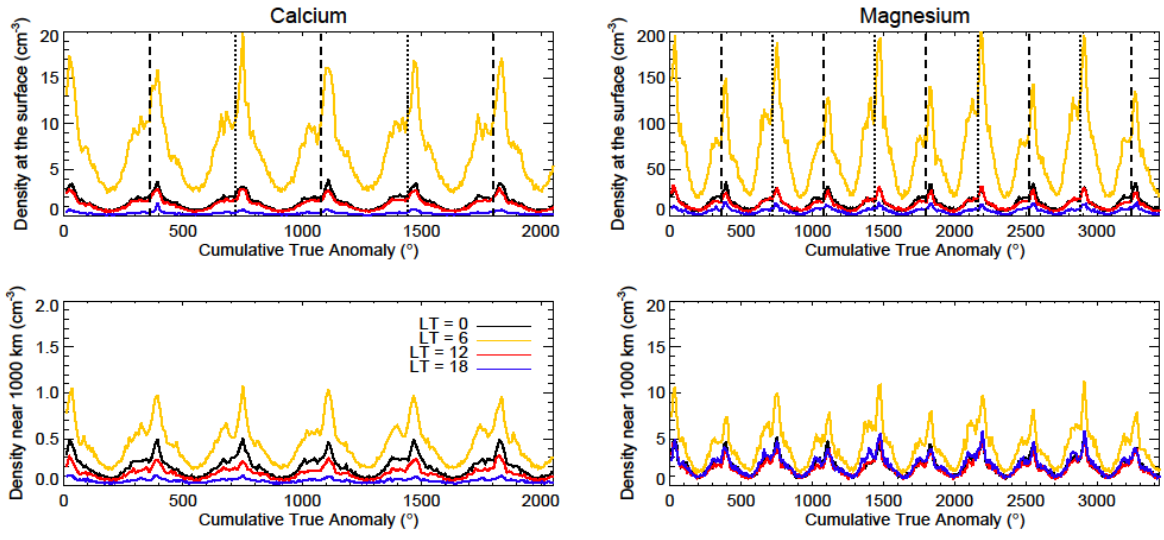

Fig. 4 : Simulated temporal variation of the Ca density (left column) and Mg (right column) at equator for different local times, near the surface (top panel) and near 1000 km (bottom panel) The vertical dashed lines and the vertical dotted lines in the top panel indicate the end of the odd and even years.

The ratio between the density at $\nu = 25°$ and $\nu = 180°$ is close to the ratio of the source at these two seasons, despite that the variation of the ionization frequency slightly reduces this ratio, particularly in the dayside at high altitude. Since the ionization lifetime (23 min near perihelion and 55 min near aphelion) is below or close to the typical time spent by a particle in the exosphere (~30 min) , the midnight density is larger than the noon density at 1000 km, while at low altitude, the densities are nearly equal due to an equal local ejection rate. This midnight/noon asymmetry is also notable in the equatorial map for $\nu \sim 0°$ (Fig. 5) and the vertical density profiles (Fig. 6). The simulated Ca tail (Fig. 5) in the planetary shadow, is not due to the radiation pressure but more to the lack of photoionization, increasing the lifetime of the exospheric Ca atoms. Such a tail is expected to be limited in extension as observed by MESSENGER during the second Mercury flyby (McClintock et al. 2009). The impact of the radiation pressure on the exospheric density is negligible (also checked it by artificially increasing the pressure by 10 without observing any significant changes of the Ca exospheric density). The radiation pressure is negligible because the ionization lifetime of a Ca atom is short ($\tau \sim 23$ min at Mercury perihelion), the radiation pressure integrated over such a short time being not efficient enough to change the trajectory of the atoms (McClintock et al. 2009).

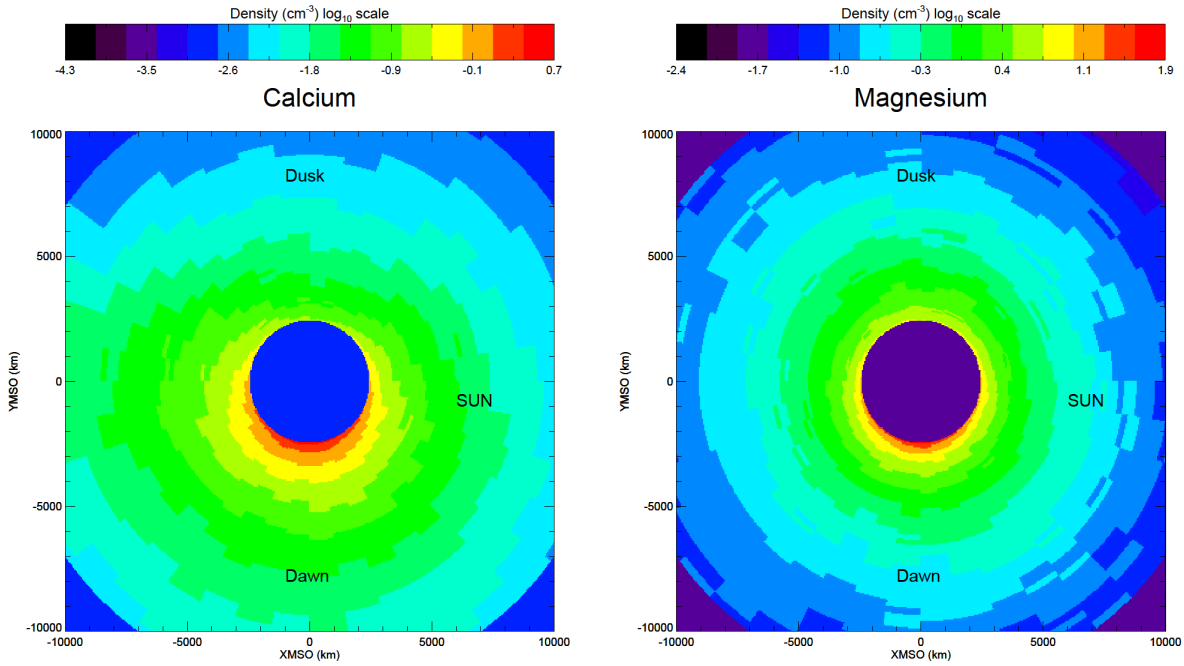

Fig. 5 Simulated Ca density (left panel) and Mg density (right panel) at a true anomaly angle $\chi = 0°$ in the XY MSO plane

Because the dust impact flux is not uniform, the ballistic horizontal (parallel to the surface) flow is not null and is directed from dawn to dusk. This horizontal flow decreases the scale height at dawn and increases it at dusk (Fig. 6). Therefore, the local scale height of the Ca density is controlled by the temperature, the horizontal flow and the ionization frequency. The numerical noise on the simulated density can be estimated from Fig. 6 showing the vertical density profiles at noon, dusk, midnight and noon, at equator for $\nu \sim 0°$ during the second and third simulated Mercury years. For Ca, there is no source of variation longer than the Mercury year in our simulations. The periodic steady state is reached at all altitudes in less than one year, and the only difference is due to the numerical statistical noise. Such noise is not important when comparing to the observations (Section 4.1.2). The simulated Ca exosphere density is not spherically symmetric. Indeed, the large ionization frequency induces a larger density at midnight above ~ 3000 km (Fig. 6). Below 1000 km the density scale height is roughly similar whereas above 1000 km, the density scale height increases from 1900 km (LT=6 am), to 2150

km (LT=12), 2500 km (LT=18) up to 3000 km at LT=0, a direct effect of the lateral transport combined with the ionization

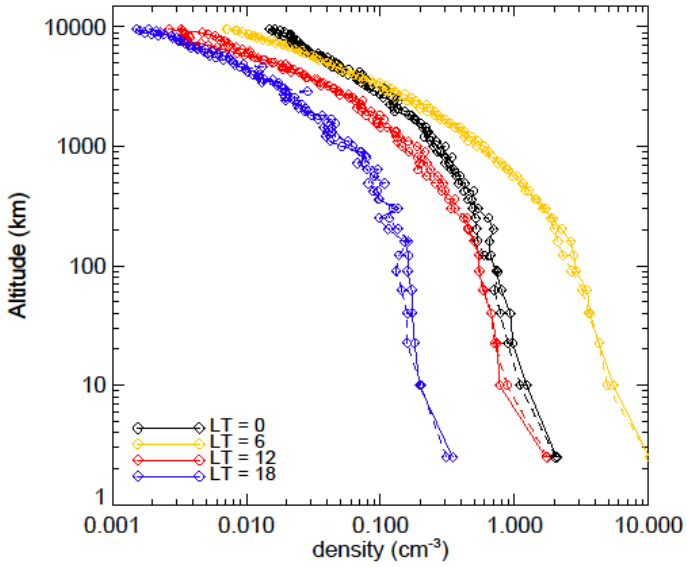

Fig. 6 Simulated Ca density profiles at ν = 0° for the second (solid lines) and third (dashed lines) simulated years at latitude =0° and four different local times.

4.1.2) Comparison with MESSENGER/MASCS

The exospheric Ca line at 422 nm is optically thin and therefore the brightness of the emission is the slant density mutliplied by the g-value (Chamberlain and Hunten 1987). The g-value has a large seasonal variation due to the Doppler effect (Killen et al. 2009), and to a lesser extent to the Mercury-Sun distance, with two peaks at ν = 60 and 300°. In the calculation of the g-values we consider an isotropic Maxwellian velocity distribution for simplification, but the simulated velocity distribution, not stored for memory reason is not isotropic as suggested by the simulated kinetic temperature. This assumption should probably be correct to ~few 10s % (Burger et al. 2014).

We use the geometry of each MASCS observations made at dawn from apoapsis (see Section 2) to compute the brightness simulated from our model.

An example of observed profile (orbit #1440, near ν = 330°) is shown in Fig. 7 with the simulated vertical brightness profiles. As noted by Burger et al. (2014), the large fraction of escaping atoms makes a scale-height based temperature quite uncertain. The small zig-zag variations are due to spacecraft motion.

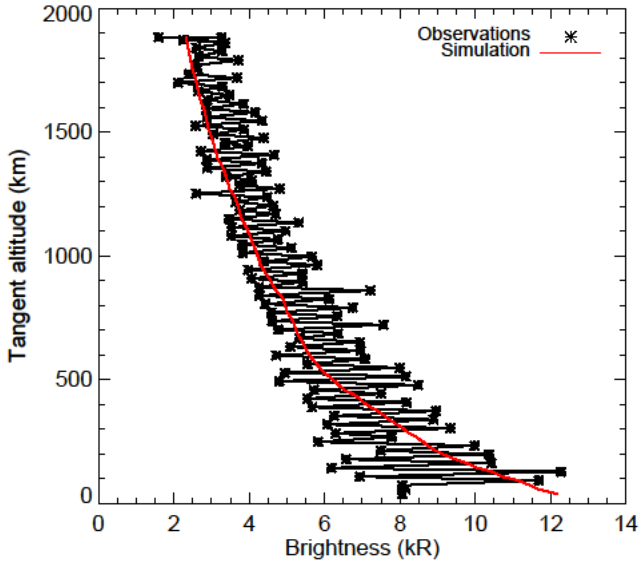

Fig. 7 Example of observed vertical profile of the Ca emission (black) and of simulated profile (red) during orbit # 1440 (v ~ 330°)

The simulated profile is in good agreement with the observation. The seasonal variation of the simulated Ca brightness near 300 km are shown in Figure 8. The observed brightness is well reproduced by the model within 30% as expected and validate our model..

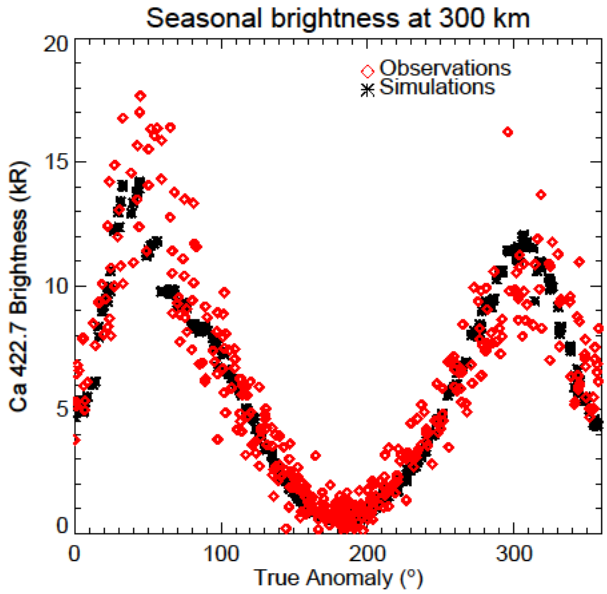

Fig. 8 Seasonal variations of the Ca brightness at dawn (6 am) for line of sight with an impact parameter near 300 km. The measured brightness is shown in red and the simulated brightness is shown in black.

4.2) Magnesium

4.2.1) Simulation results

Several Mercury years were simulated. As for Ca a periodic steady state is reached during the first year (Fig. 4), but the Mg simulation includes an additional two-year period compared to the Ca simulated exosphere due to the non-uniform Mg surface density considered in our simulations. Seasonal variations of the Mg density are similar to Ca variations due to the variation of the dust impact flux, with a minimum of density near $\nu = 180°$ and a maximum of density at $\nu = 25°$. Noise due to statistics in the Monte Carlo simulations are the cause of the short time scale variations.

Near the surface, the biennial cycle is significant at dawn but is less significant at dusk (Fig. 4). At dusk, a large fraction of the Mg atoms in the exosphere, even near the surface, are not

364 produced locally but are transported from dawn. Therefore, the local increase of the production
365 at dusk during the end of odd years (ν=385°, 1105°, 1865°, …) is balanced by the decrease of
366 the Mg atoms coming from dawn. A similar effect can explain the noon/midnight variation with
367 a two-year cycle of the density near the surface at noon but not at midnight (the local production
368 and the supply from dawn increase at noon at ν = 25°, 745°, 1465°, etc., while at midnight the
369 local production decreases at ν = 25°, 745° balancing the increase of the supply from dawn). At
370 1000 km, the biennial cycle is observed at all local times, although it is smaller at dusk, noon
371 and midnight than at dawn. Above 1000 km, the density is more sensitive to the integrated
372 source rate over the surface which is only 10% larger when the Mg enriched region is near dawn
373 at the beginning of the odd years (ν = 25°, 745°, 1465°, …) than near dusk at the beginning of
374 the even years (ν = 385°, 1105°, 1825°, …).

375 Because the ionization lifetime of Mg (between 40 and 100 hours) is much larger than the
376 ionization lifetime of Ca, the photoionization impact on the exospheric density is negligible,
377 and the density near noon and midnight remains comparable at 1000 km altitude. The equatorial
378 map of the Mg density at ν = 360° is shown in Fig. 5, the radiation pressure, included in our
379 simulations is not efficient enough to create a noticeable extended tail on the nightside (Fig.
380 10), but is sufficient to increase the average time of residence of the atoms in the exosphere,
381 creating a small dayside/nightside asymmetry. Contrary to the Ca simulation, a simulation
382 performed with an arbitrary 10 times larger radiation pressure showed the formation of a Mg
383 tail.

384

385 A way to prove that a large fraction of Mg atoms in the exosphere at dusk are coming from
386 dawn and not from the dusk surface is to estimate the simulated kinetic temperature. In the
387 simulation, all the Mg atoms are ejected with a MBF distribution at T = 6000 K. At LT= 12h
388 and 24h, the simulated kinetic temperature near the surface is close to 6000K. At LT = 6h it is

389 slightly lower (5500 K), while at LT = 18h, the kinetic temperature is slightly larger (8500 K)
390 (Fig. 9). At dawn the temperature is reduced by the diverging flow of Mg atoms from dawn to
391 dusk. From a kinetic approach, Mg atoms initially ejected with a large horizontal (parallel to
392 the surface) velocity are moving from dawn to dusk, this local loss of the Mg atoms is not
393 balanced by atoms coming from dusk because of the lower production rate. Therefore, the dawn
394 should be relatively depleted of atoms with with large horizontal velocity leading to a smaller
395 width of the velocity distribution function. On the contrary, the small fraction of particles
396 moving from dawn to dusk represent a substantial fraction of the atoms present at dusk.
397 Therefore, the dusk velocity distribution function should be enriched at large horizontal velocity
398 at dusk, leading to an increase of the kinetic temperature.

399 This effect is very general in collisionless medium, and can be noted, for example, in the
400 simulations of the hot oxygen in the exosphere of Mars by Hodges (2000) where the simulated
401 kinetic temperature at noon (the maximum of production of hot oxygen) is lower than the
402 simulated kinetic temperature at midnight (the minimum of production of hot oxygen).

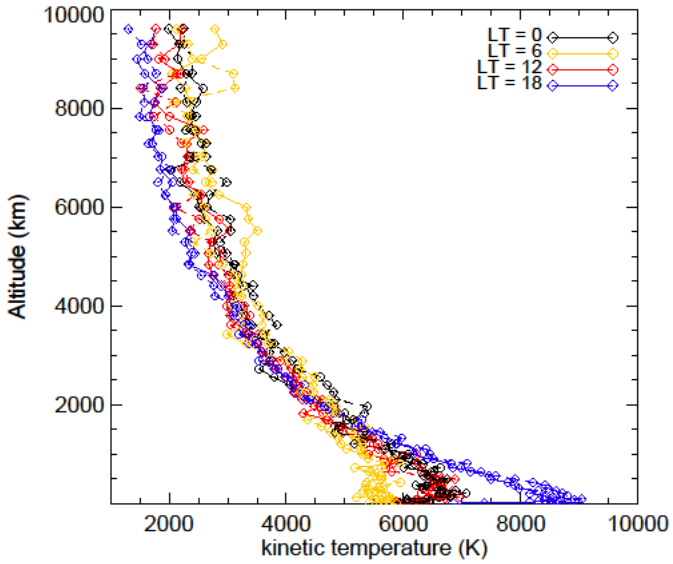

403

404 *Fig. 9 Simulated Mg kinetic temperature profiles at v = 0° for the second (solid lines) and*
405 *third (dashed lines) simulated years at latitude =0° and four different local times*

406 This confirms that a substantial fraction of the atoms present in the exosphere at dusk near the
407 surface (in the equatorial plane) are energetic atoms with an initial horizontal velocity large
408 enough to travel balistically from dawn (the peak of ejected Mg atoms) to dusk.

409 The vertical profiles of the simulated density are shown in Fig. 10. The simulated Mg density
410 is ~ 10 larger than the simulated Ca density near the surface.

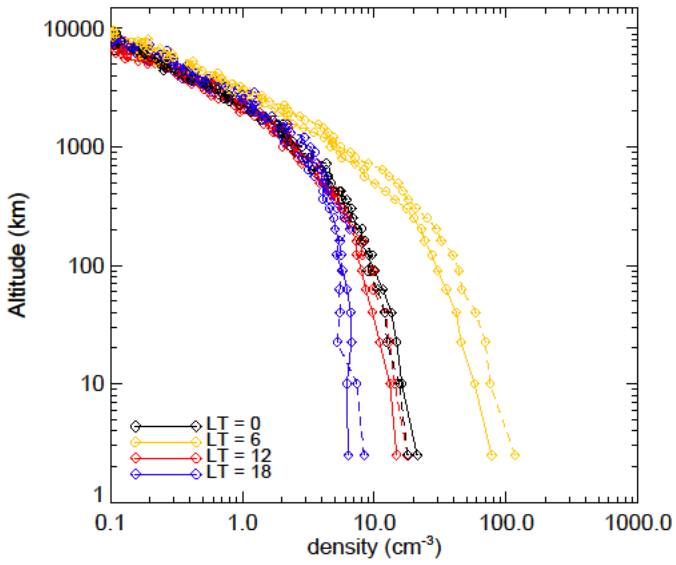

411

412 *Fig. 10 Simulated Mg density profiles at v = 0° for the second (solid lines) and third (dashed*
413 *lines) simulated years at latitude =0° and four different local times.*

414 At dawn and noon, the variation of the simulated density between the two years displayed in
415 Fig. 10 is due to the biennial cycle discussed before and not to the numerical noise. At higher
416 altitudes (> 2000 km), the Mg exosphere becomes nearly spherically symmetric, even though
417 the radiation pressure produces a small night/day asymmetry (see also Fig. 5). As for Ca, the
418 lateral flow decreases the scale height at dawn and increases it at dusk (Fig. 10). Note that,
419 despite the lower kinetic temperature mass ratio (expressed in Dalton (Da) or atomic mass unit)
420 for Mg (~247K/Da) than Ca (1745 K/Da), the Mg and Ca density decreases by a similar factor
421 of ~ 100 – 1000 from the surface to 10,000 km, confirming the importance of the ionization
422 frequency in the scale height of the Ca density. The Mg dawn/dusk density ratio near 300 km

423 is between 2 – 3, lower than the Ca dawn/dusk ratio near 300 km (~ 10) (Fig.6). Compared to
424 Mg, a smaller fraction of Ca atoms produced near dawn reach the dusk side due to the shorter
425 Ca ionization lifetime.

426

427 4.2.2) Comparison with MESSENGER/MASCS

428 We also compare systematically all the observations by MESSENGER to the simulated density
429 assuming an optically thin emission (Fig. 11). The seasonal variations of the excitation
430 frequency used in our manuscript differ from Merkel et al. (2017) as discussed in Section 5.

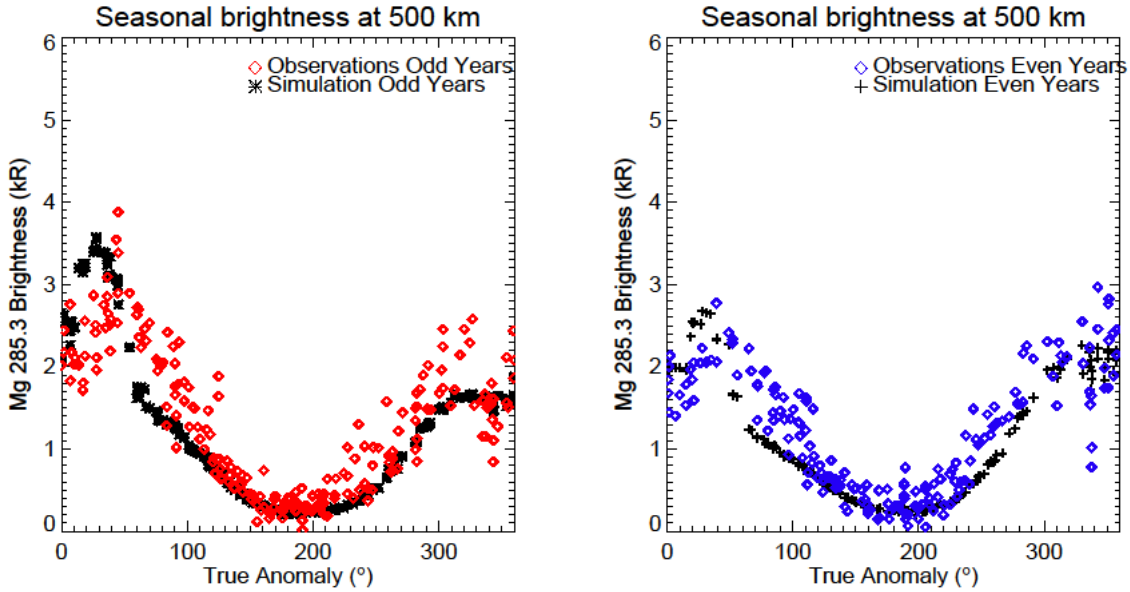

431

432 *Fig. 11 Seasonal variations of the Mg brightness at dawn (6 am) for line of sight with an impact*
433 *parameter near 500 km for odd (left figure) and even (right figure) years The measured*
434 *brightness is shown in red (odd years) and blue (even years) and the simulated brightness is*
435 *shown by black diamonds (odd years) and black crosses (even years).*

436 This comparison shows a good agreement, within 30% of the seasonal variations between the
437 observations and simulated brightness for $\nu > 80°$ where the dust flux from Encke is negligible.
438 The observed biennial cycle is also reproduced.

439 This result confirms that the interplanetary dust impact is the main source of both calcium and
440 magnesium ejection in the exosphere of Mercury and the two set of observations are consistent
441 with a source due to an interplanetary dust disk with geometrical parameters published by Killen
442 and Hahn (2015) for $\nu > 80°$. There is a small discrepancy between the Mg simulation and the
443 observations between $\nu = 20°$ and $\nu = 80°$, where the additional source attributed to Encke dust
444 flux is important. As explained in Section 5, the simulated brightness is very sensitive to the
445 excitation frequency of the Mg line which uncertainty might explain this discrepancy.

446 **5) Discussion**

447 5.1) Mg g-value

448 The seasonal variations of the Mg g-value used to simulate the Mg brightness are shown in Fig.
449 12b and are calculated using the solar spectrum measured by the Air Force Geophysical
450 Laboratory (Hall and Aderson 1991), sampled every 100 mA, but rescaled in flux by a factor
451 0.83 (Langowski et al. 2014). We also consider a maxwellian velocity distribution at a fixed
452 temperature (T = 6000K for Mg). This assumption is not correct because the simulated velocity
453 distribution is not maxwellian but the non-maxwellian effect are not expected to be large. For
454 example, if we neglect completely the velocity of the atoms in Mercury frame (i.e. used a Dirac
455 velocity distribution at V = 0 in Mercury's frame), the comparison is not modified substantially
456 for Mg.

457 The seasonal variations of the g-values differ from the variations used by Merkel et al. (2017)
458 (dashed line). The difference is due to the solar spectral flux used to compute the g-value (Fig.
459 12a). Merkel et al. (2017), used the high spectral resolution solar flux from Killen et al. (2009).
460 The spectrum of Killen et al. (2009) has a better spectral resolution (10 mA) but contains a
461 feature near 285.3 nm not present in the solar spectrum of Hall and Anderson (1991). This
462 feature is the main source of difference between our g-values and the g-value of Merkel et al.
463 (2017). This feature is not due to the better spectral resolution of the solar spectrum of Killen

et al. (2009). The dot-dashed line in Fig 12a corresponds to the solar spectrum from Killen et al. (2009) degraded to 100 mA resolution. It shows that with a resolution of 100 mA, the feature near 285.3 nm should have been detected. Then the solar spectrum from Hall and Anderson (1991) and Killen et al. (2009) are not consistent in this spectral range. This difference has a large effect on the interpretation of the seasonal variation of the Mg brightness and therefore, new high spectrally resolved solar spectrum in this wavelength range is highly needed. The recently published solar spectrum from Coddington et al. (2021) also used the observations done by Hall and Anderson (1991) between 200 and 310 nm rescaled in flux close to 0.83 (Fig. 12a). The solar spectrum of Chance and Kuruzc (2010) is systematically larger in this wavelength range by ~ 1.5.

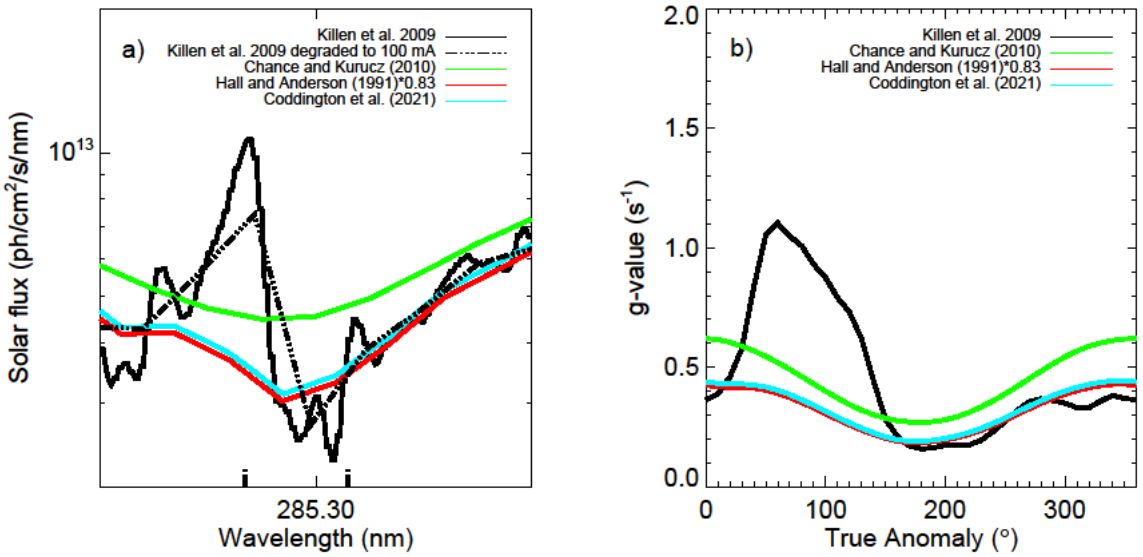

Fig. 12 a) Solar spectrum near 285. 3 nm used in the simulation compared to other solar spectrum. The two vertical dot-dashed lines on the x-axis represent the Doppler shifted wavelength range due to the radial velocity of Mercury (~±10 km/s) along its orbit. b) Seasonal variations of the g-value of the Mg line used in our simulations, compared to the g-value derived from other solar flux.

Also, it should be noted that the FWHM of the MASCS instrument was 6.6 Å much larger than the resolution of all these solar features.

The spectral resolution of the observed solar spectrum from Hall and Anderson (1991) and then, the spectrum from Chance and Kuruzc (2010) or Coddington et al. (2021) are not sufficient to derive accurately the seasonal variation of the Mg g-value at Mercury (Fig. 12a) and may explain the remaining difference for $\nu < 80°$. A deeper Fraunhofer line, would decrease the excitation frequency at $\nu = 0°$ and $\nu = 180°$ and shift the g excitation frequency peak towards $\nu = 90°$ and $\nu = 270°$, leading to a better fit of the observations.

Contrary to Mg, the seasonal variations of the g-value for Ca derived from the solar spectrum of Killen et al. (2009) are in very good agreement with those derived from Coddington et al. (2021) and then not discussed.

5.2) Ca and Mg ejection rates

The simulated Mg and Ca vaporization rates are given by Eq. 1 as the product of the impacting dust flux, the X/Si surface ratio and a free parameter *A*. This free parameter *A* was tuned to fit the Ca observations and this same value is used for Mg and give a good fit of the MESSENGER observations (Fig. 11). For Ca, we consider a uniform surface distribution of Ca/Si = 0.15, which is a simplification, since the MESSENGER/XRS show some variations from 0.05 to 0.3, but with an incomplete coverage. Such variations may cause a biennial cycle in the exospheric Ca, but possibly of too small magnitude to be detected by MESSENGER/MASCS. We implicitly assume that all Ca and Mg atoms ejected into the exosphere of Mercury are coming from the surface of Mercury. In reality, a fraction of the exospheric Ca and Mg atoms could come from the impacting dust itself but the volume of impact melt and vapor should be much larger than the impactor volume (Cintala 1992). Ca and Mg are ejected under molecular form and should be quickly dissociated in the dayside (Cassidy et al. 2021). Therefore, the production of atomic Ca and Mg should not be exactly at the surface. Such complexity will be considered in the future. The simulated Ca and Mg ejection rates at 6 am are displayed in Fig. 13.

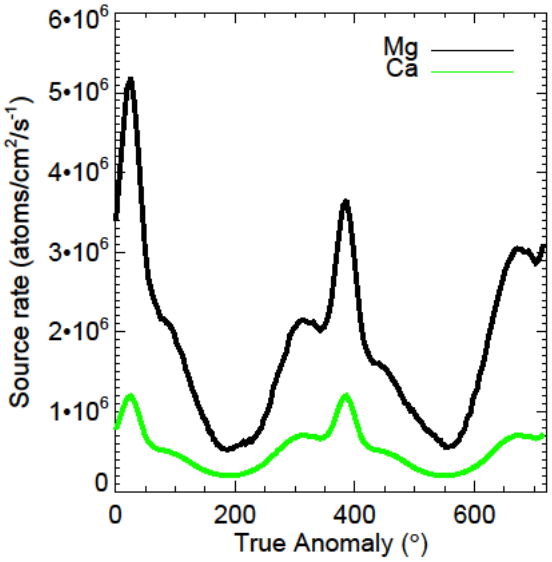

506

507 *Fig. 13 Simulated seasonal variations of the Mg and Ca source rate at latitude =0°, LT = 6*
508 *am*

509 For Ca, we found a systematic lower source rate by a factor of 2 compared to Burger et al.
510 (2014). This difference is not understood since the assumptions used in our model are those
511 used by Burger et al. (2014).

512 For Mg, the ejection rate at dawn are larger by a factor of ~4 - 10 compared to the ejection
513 rate derived by Merkel et al. (2017) near dawn. A cause of the difference is associated to the
514 g-values used by Merkel et al. (2017) to derive the source rate near $\nu = 60°$.But even for $\nu >$
515 140°, where the g-value used by Merkel et al. (2017) is close to the value used in our study
516 (Fig. 12b) there is a systematic difference by a factor of ~ 5. The use of a non-uniform source
517 rate is the main cause of the discrepancy. Merkel et al. (2017) used a 1D Chamberlain model,
518 so the horizontal flow of particles ejected at dawn is exactly balanced by particles ejected
519 elsewhere and moving to dawn. In our simulations, this horizontal flow is not balanced
520 because the ejection rate is lower at other local times and therefore, to compensate the lateral
521 loss and fit the observations, the source rate should be increased compared to a 1D simulation.

522 The ratio between the Mg and Ca ejection rate follows the Mg/Ca ratio at the surface of
523 Mercury but since we use a homogeneous surface concentration for Ca and a heterogeneous
524 surface concentration for Mg, a biennial cycle is simulated for Mg but not for Ca.

525 **6) Conclusion and future work**

526 We use the LATMOS Exospheric Global Model to study Ca and Mg emissions observed by
527 UVVS/MESSENGER, focusing on the dawn observations. Our study shows that the seasonal
528 variations for true anomaly angle $\nu > 80°$ of the two species can be explained by impact
529 vaporization from interplanetary dust coming from a disk with the geometric properties
530 proposed by Killen and Hahn (2015). For Ca an additional source, attributed to Encke dust by
531 Killen and Hahn (2015) is needed with a peak near $\nu = 25°$ and could be sufficient to reproduce
532 the Mg observations. This last result strongly depends on the depth of the solar Fraunhofer line
533 corresponding to the Mg emission wavelength not well known due to the limited spectral
534 resolution of the solar flux near 285 nm. Physical processes important near $\nu = 0°$, not included
535 in our models could also be the cause of the discrepancy. We also found that due to the large
536 dawn/dusk asymmetry in the source rate, 1D models are not adapted to intepret the observations
537 and derive the source flux with a good accuracy because this large asymmetry produces a strong
538 horizontal circulation from dawn (the source maximum) to dusk (the source minimum), and
539 then affect the local density scale heights and source rate needed to reproduce the observations.
540 Our model is probably still too simple to catch all the observed variations. A more accurate
541 model of the dust impact flux as developed by Pokorny et al. (2018) shows some seasonal
542 variations of the local time of the peak of the dust impact flux (slightly shifted towards midnight
543 for $\nu < 180°$ and towards noon for $\nu > 180°$) that could slightly affect the seasonal variations at
544 different local times. Other effects not considered in this study that will be considered in the
545 future are the amount of Ca/Mg coming from Mercury and the dust as well as a study of the
546 local time variations that could help to better constrain the origin of the dust responsible of the

547 formation of the Mg/Ca exosphere of Mercury. These two species are in the spectral range of
548 the instrument PHEBUS onboard BepiColombo (Quémerais et al. 2020) and are expected to be
549 regularly observed during one terrestrial year after the insertion of the spacecraft around
550 Mercury. Those measurements would help to better understand the origin of these two species.

551 **Acknowledgements**
552 We thank CNES for their support of this study. MESSENGER/MASCS data reported in this
553 paper are archived by the NASA Planetary Data System : https://pds-
554 geosciences.wustl.edu/missions/messenger/mascs.htm. The Mg/Si map produced by
555 MESSENGER/XRS is archived by the NASA PDS https://pds-
556 geosciences.wustl.edu/missions/messenger/xrs.htm

557 Simulated Mg and Ca density for two Mercury years (simulated Years 2 and 3) can be found in
558 zenodo (doi: https://doi.org/10.5281/zenodo.5575812)
559 The solar flux used to simulate the Mg g-value is archived on the NOAA ftp repository:
560 ftp.ngdc.noaa.gov/STP/SOLAR_DATA/SOLAR_UV/MID_UV
561
562
563

564 **Appendix : Relation between MSO and planetographic coordinates**

565 In this appendix, the Mercury-Sun distance will be noted r instead of d (in the manuscript) to
566 avoid confusion with the differential operator. The planetocentric longitude α can be derived
567 from the MSO longitude φ at any time by integration of the orbital motion of Mercury (Eq. A1)

568 $$\varphi(\alpha, t) = \varphi(\alpha, 0) + \frac{180}{\pi}\int_0^t (\omega_{rot} - \omega_{orb}(t'))dt' \qquad \text{(Eq. A1)}$$

569 The areal velocity is constant (2nd Kepler's law) and given by

$$V_A = \frac{1}{2} r^2 \omega_{orb}(t) = \frac{1}{2} r^2 \frac{dv}{dt} \quad \text{(Eq. A2)}$$

In the integration, the time variable t can be replaced by the TAA ν

$$dt = \frac{1}{2} \frac{r^2}{V_A} dv \quad \text{(Eq. A3)}$$

$$\varphi(\alpha, v) = \varphi(\alpha, 0) + \frac{180}{\pi} \int_0^v \left(\frac{r^2(v')}{2V_A} \omega_{rot} - 1 \right) dv' \quad \text{(Eq. A4)}$$

By convention, we choose the initial condition φ(α, 0) = α for odd years and φ(α, 0) = 180°+α for even years.

The second term inside the parenthesis can be integrated directly to obtain

$$\varphi(\alpha, \nu) = \varphi(\alpha, 0) + \frac{180}{\pi} \left[\int_0^v \left(\frac{r^2(v')}{2V_A} \omega_{rot} \right) dv' - v \right] \quad \text{(Eq. A5)}$$

The Mercury orbit around the sun is an ellipse defined by a polar coordinate equation:

$$r(v) = \frac{p}{1 + e \cos v} \quad \text{(Eq. A6)}$$

Replacing r(ν) by this expression in the integral leads to

$$\int_0^v \left(\frac{r^2(v')}{2V_A} \omega_{rot} \right) dv' = \frac{p^2 \omega_{rot}}{2V_A} \int_0^v \frac{dv\prime}{(1 + e \cos v\prime)^2} \quad \text{(Eq. A7)}$$

The areal velocity is constant and equal to the area swept out during a full orbit (πab), where a and b are the semi-major axis and the semi-minor-axis respectively, divided by the orbital period : $2\pi/\langle\omega_{orb}\rangle$

For an ellipse : $p = a(1-e^2)$ and $p = b(1-e^2)^{1/2}$. The products p^2 is then equal to $ab(1-e^2)^{3/2}$, and then

$$\frac{p^2 \omega_{rot}}{2V_A} = (1 - e^2)^{3/2} \frac{\omega_{rot}}{\langle \omega_{orb} \rangle} \quad \text{(Eq. A8)}$$

589 A way to calculate the integral A7 is to multiply by 1= (1-e^2 +ecosv' – ecosv')/(1-e^2) and

590 separate in two terms

591 $$\int_0^{\nu} \frac{d\nu'}{(1+e\cos\nu')^2} = \frac{1}{1-e^2}\int_0^{\nu} \frac{(1-e^2+e\cos\nu'-e\cos\nu')d\nu'}{(1+e\cos\nu')^2} \qquad \text{(Eq. A9)}$$

592 $$\int_0^{\nu} \frac{d\nu'}{(1+e\cos\nu')^2} = \frac{1}{1-e^2}\int_0^{\nu} \left(\frac{1}{1+e\cos\nu'} - \frac{e^2+e\cos\nu'}{(1+e\cos\nu')^2}\right) d\nu' \qquad \text{(Eq. A10)}$$

593 The second integration can be easily calculated.

594 $$\int_0^{\nu} \left(\frac{e^2+e\cos\nu'}{(1+e\cos\nu')^2}\right) d\nu' = \frac{e\sin\nu}{1+e\cos\nu} \qquad \text{(Eq. A11)}$$

595 The first integration is a fraction is cos(ν) which can be solved by the usual method using the

596 variable x = tan(ν/2), dν = 2dx/(1+x^2) , cos(ν) = (1-x^2)/(1+x^2)

597 $$\int_0^{\nu} \left(\frac{1}{1+e\cos\nu'}\right) d\nu' = \frac{2}{1+e}\int_0^{\tan(\frac{\nu}{2})} \frac{2dx}{1+x^2\frac{1-e}{1+e}} = \frac{2}{\sqrt{1-e^2}}\int_0^{\sqrt{\frac{1-e}{1+e}\tan(\frac{\nu}{2})}} \frac{dy}{1+y^2} \qquad \text{(Eq. A12)}$$

598 where a last variable change y = (1-e)$^{1/2}$/(1+e)$^{1/2}$x was used to derive the last expression.

599 When ν < π the integral can ne calculated directly (the upper variable is always lower than

600 infinity) and leads to

601 $$\int_0^{\nu} \left(\frac{1}{1+e\cos\nu'}\right) d\nu' = \frac{2}{\sqrt{1-e^2}} tan^{-1}\left(\sqrt{\frac{1-e}{1+e}}\tan(\frac{\nu}{2})\right) \qquad \text{for } \nu < \pi \qquad \text{(Eq. A13)}$$

602 When ν > π we need to use the Chasles relation :

603 $$\int_0^{\nu} \left(\frac{1}{1+e\cos\nu'}\right) d\nu' = \int_0^{\pi} \left(\frac{1}{1+e\cos\nu'}\right) d\nu' + \int_{\pi}^{\nu} \left(\frac{1}{1+e\cos\nu'}\right) d\nu' \qquad \text{(Eq.A14)}$$

604 The first integral can be computed from A13:

605 $$\int_0^{\pi} \left(\frac{1}{1+e\cos\nu'}\right) d\nu' = \frac{\pi}{\sqrt{1-e^2}} \qquad \text{(Eq. A15)}$$

606 The last integral can be calculated replacing ν by ν– π which leads to

607 $$\int_{\pi}^{\nu} \left(\frac{1}{1+e\cos\nu'}\right) d\nu' = \int_0^{\nu-\pi} \left(\frac{1}{1-e\cos\nu'}\right) d\nu' \qquad \text{(Eq. A16)}$$

608 This integral can be solved as A12 (replacing e by -e)

609 $$\int_0^{\nu-\pi}\left(\frac{1}{1-ecos\nu'}\right)d\nu' = \frac{2}{\sqrt{1-e^2}}\int_0^{\sqrt{\frac{1+e}{1-e}}\tan(\frac{\nu-\pi}{2})}\frac{dy}{1+y^2}$$ (Eq. A17)

610 Finally, we found

611 $$\int_0^{\nu}\left(\frac{1}{1+ecos\nu'}\right)d\nu' = \frac{\pi}{\sqrt{1-e^2}} + \frac{2}{\sqrt{1-e^2}}tan^{-1}\left(\sqrt{\frac{1+e}{1-e}}\tan(\frac{\nu-\pi}{2})\right)$$ for $\nu > \pi$ (Eq. A18)

612 Using, Eq. A5, A7, A8, A11 and A13 leads to Eq. 6a and using Eq A5, A7, A8, A11 and A18
613 leads to Eq 6b.

614

615

616 **References**

617 Bida, T.A., R.M. Killen, and T.H. Morgan, Discovery of calcium in Mercury's atmosphere,
618 Nature, 404, 159-161, doi :10.1038/35004521, (2000)

619 Broadfoot, A.L., D.E. Shemansky, and S. Kumar, Mariner 10 : Mercury atmosphere, Geophys.
620 Res. Lett., 3, 577-580, (1976)

621 Burger, M.H., R.M. Killen, W.E. McClintock, R.J. Vervack, A.W. Merkel, A.L. Sprague, M.
622 Sarantos, Modeling MESSENGER observations of calcium in Mercury's exosphere, J.
623 Geophys. Res., 117, E00L11, doi : 10.1029/2012JE004158, 2012

624 Burger, M.H., R.M. Killen, W.E. McClintock, R.J. Vervack, A.W. Merkel, T.A. Cassidy, M.
625 Sarantos, Seasonal variations in Mercury's dayside calcium exosphere, Icarus, 238, 51-
626 58, (2014)

627 Bzowski, M., On the importance of the stochastic character of the radiation pressure in
628 exospheric modelling, Ann. Geophys., 11, 150-159, (1993)

629 Cassidy, T.A., C.A. Schmidt, A.W. Merkel, J.M. Jasinski, and M.H. Burger, Detection of large
630 exospheric enhancements at Mercury due to meteoroid impacts, Planet. Sci., 2, 175,
631 (2021)

632 Chamberlain, J.W., Planetary coronae and atmospheric evaporation, Planet. Space Sci., 11,
633 901-960, doi :10.1016/0032-0633(63)90122-3, (1963)

634 Chamberlain, J.W. and D. Hunten, Theory of planetary atmospheres: An introduction to their
635 physics and chemistry, International Geophys. Ser., 36, Academic Press Inc Florida,
636 (1987)

637 Chance, K., and R.L. Kurucz, An improved high-resolution solar reference spectrum for earth's
638 atmosphere measurements in the ultraviolet, visible, and near infrared, J. Quant. Spec.
639 and Rad. Transf., 111, 1289-1295 (2010)

640 Christou, A.A., R.M. Killen, and M.H. Burger, The meteoroid stream of comet Encke at
641 Mercury : Implications for MErcury Surface, Space ENvironment, GEochemsitry, and
642 Ranging observations of the exosphere, Geophys. Res. Lett., 42, 7311-7318, doi :
643 10.1002/2015GL065361, (2015)

644 Coddington, O.M., E.C. Richard, D. Harber, P.Pilewskie, T.N. Woods, K. Chance, X. Liu, and
645 K. Sun, The TSIS Hybrid solar reference spectrum, Geophys. Res. Lett., 48,
646 e2020GL091709, doi: 10.1029/2020GL091709, (2021)

647

648 Grava, C., R. M. Killen, M. Benna, A. Berezhnoy, J. S. Halekas, F. Leblnc, M. N.
649 Nishino, C. Plainaki, J. M. Raines, M. Sarantos, B. D. Teolis, O. J. Tucker, R. J.
650 Vervack, Jr., and A. Vorburger, Volatiles and refractories in surface-bounded
651 exospheres in the inner solar system. Space Science Reviews. SPAC-S-20-00147,
652 2021. 10.1007/s11214-021-00833-8

653 Hall, L.A., and G.P. Anderson, High-resolution solar spectrum between 2000 and 3100 Å, J.
654 Geoophys. Res., 96, 12,927-12,931, (1991)

655 Hodges, R.R., Distributions of hot oxygen for Venus and Mars, J. Geophys. Res., 105, 6971-
656 6981, (2000)

657 Killen, R.M., Pathways for energization of Ca in Mercury's exosphere, Icarus, 268, 32-36,
658 (2016)

659 Killen, R.M., and J.M. Hahn, Impact vaporization as a possible source of Mercury's calcium
660 exosphere, Icarus, 250, 230-237, (2015)

661 Killen, R.M. T.A. Bida, and T.H. Morgan, The calcium exosphere of Mercury, Icarus, 173,
662 300-311, doi :10.1016/j.icarus.2004.08.022, (2005)

663 Killen, R.M., G. Cremonese, H. Lammer, S. Orsini, A.E. Potter, A.L. Sprague, P. Wurz, M.L.
664 Khodachencko, H. I. M. Lichtenegger, A. Millilo, and A. Mura, Processes that promote
665 and deplete the exosphere of Mercury, Space Sci. Rev., 132, 433-509, doi :
666 10.1007/s11214-007-9232-0, (2007)

667 Killen, R.M, D. Shemansky, and N. Mouawad, Expected emission from Mercury's exospheric
668 species and their ultraviolet-visible signatures, Astrophys. J. Supp. Series, 181, 351-359,
669 (2009)

670 Killen, R.M., M.H. Burger, R.J. Vervack, and T.A. Cassidy, Understanding Mercury's
671 Exosphere: Models derived from MESSENGER observations, The view after
672 MESSENGER, ed. by S. Solomon, L. Nittler, B. Anderson. Cambridge Planetary
673 Science, (Cambridge University Press, Cambridge 2018), 407-429, doi:
674 10.1017/9781316650684.016, (2018)

675 Langowski, M., M. Sinnhuber, A.C. Aikin, C. von Savigny, and J.P. Burrow, Retrieval
676 algorithm for densities of mesospheric and lower thermospheric metal atom and ion

677 species from satellite-borne limb emission signals, Atmos. Meas. Tech., 7, 29-48,
678 (2014)

679 Leblanc, F., E. Chassefière, R.E. Johnson, D.M. Hunten, E. Kallio, D.C. Delcourt, R.M. Killen,
680 J.G. Luhmann, A.E. Potter, A. Jambon, G. Cremonese, M. Mendillo, N. Yan, and A.L.
681 Sprague, Mercury's exosphere origin and relations to its magnetosphere and surface,
682 Planet. Space Sci., 55, 1069-1092, (2007)

683 Leblanc, F., J-Y. Chaufray, A. Doressoundiram, J-J. Berthelier, V. Mangano, A. Lopez-Ariste,
684 and P. Borin, Mercury exosphere : III Energetic characterization of its sodium
685 component, Icarus, 223, 963-974, (2013)

686 Leblanc, F., J-Y. Chaufray, R. Modolo, L. Leclercq, S. Curry, J. Luhmann, R. Lillis, T. Hara,
687 J. McFadden, J. Halekas, N. Schneider, J. Deighan, P.R. Mahaffy, M. Benna, R.E.
688 Johnson, F. Gonzalez-Galindo, F. Forget, M.A. Lopez-Valverde, F.G. Eparvier, and B.
689 Jakosky, On the origins of Mars' exospheric nonthermal oxygen component as observed
690 by MAVEN and modeled by Heliosares, J. Geophys. Res. : Planets, 122, 2401-2428,
691 (2017a)

692 Leblanc, F., A.V. Oza, L. Leclercq, C. Schmidt, T. Cassidy, R. Modolo, J-Y. Chaufray, and
693 R.E. Johnson, On the orbital variability of Ganymede's atmosphere, Icarus, 293, 185-
694 198, (2017b)

695 Leblanc, F., C. Schmidt, V. Mangano, A. Mura, G. Cremonese, J. Raines, J. M.
696 Jasinski, M. Sarantos, A. Milillo, R. Killen, T. Cassidy, R. Vervack, S. Kameda, M.
697 Horanyi, D. Janches, A. Berezhnoy, A Christou, T. Hirai, P. Lierle, and J.
698 Morgenthaler, Comparative Na and K Mercury and Moon exospheres, Space
699 Science Reviews (under review)

McClintock, W. E. and Lankton, M. R. The Mercury Atmospheric and Surface Composition Spectrometer for the MESSENGER mission. Space Sci. Rev., 131, 481–521, doi:10.1007/s11214-007–9264-5., (2007)

McClintock, W. E., Bradley, E. T., Vervack, R. J., Jr., Killen, R. M., Sprague, A. L., Izenberg, N. R. and Solomon, S. C. . Mercury's exosphere: Observations during MESSENGER's first Mercury flyby. Science, 321, 92–94., (2008)

McClintock, W. E., Vervack, R. J., Bradley, E. T., Killen, R. M., Mouawad, N., Sprague, A. L., Burger, M. H., Solomon, S. C. and Izenberg, N. R., MESSENGER observations of Mercury's exosphere: Detection of magnesium and distribution of constituents. Science, 324, 610–613, doi:10.1126/science.1172525, (2009)

McClintock, W.E., T.A. Cassidy, A.W. Merkel, R.M. Killen, M.H. Burger, and R.J. Vervack Jr, Observations of Mercury's exosphere : Composition and structure, in Mercury : The view after MESSENGER, ed. by S. Solomon, L. Nittler, B. Anderson. Cambridge Planetary Science, (Cambridge University Press, Cambridge 2018), 371-406, doi :10.1017/9781316650684.015

Merkel, A.W., T.A. Cassidy, R.J. Vervack, W.E. McClintock, M. Sarantos, M.H. Burger, R.M. Killen, Seasonal variations of Mercury's magnesium dayside exosphere from MESSENGER observations, Icarus, 281, 46-54, (2017)

Merkel, A.W., J.R. Vervack, R.M. Killen, T.A. Cassidy, W.E. McClintock, L.R. Nittler, and M.H. Burger, Evidence of connection Mercury's magnesium exosphere to its magnesium-rich surface terrane. Geophys. Res. Lett., 45, 6790-6797, doi :10.1029/2018GL078407, (2018)

722 Oza, A. V., F. Leblanc, R.E. Johnson, C. Schmidt, L. Leclercq, T.A. Cassidy, and J-Y.
723 Chaufray, Dusk over dawn O2 assymmetry in Europa's near surface atmosphere, Planet.
724 Space Sci., 167, 23-32, (2019)

725 Pokorny, P., M. Sarantos, and D. Janches, A comprehensive model of the meteoroids
726 environment around Mercury, Astrophys. J., 863, 31, (2018)

727 Potter, A.E., and T.H. Morgan, Discovery of sodium in the atmosphere of Mercury, Science,
728 229, 651-653, doi :10.1126/science.229.4714.651 (1985)

729 Quémerais, E., J-Y. Chaufray, D. Koutroumpa, F. Leblanc, A. Réberac, B. Lustrument, C.
730 Montaron, J-F. Mariscal, N. Rouanet, I. Yoshikawa, G. Murakami, K. Yoshioka, O.
731 Korablev, D. Belyaev, M.G. Pelizzo, A. Corso, P. Zuppella, PHEBUS on Bepi-
732 Colombo: Post-launch update and instrument performance, Space Sci. Rev., 216:67,
733 (2020)

734 Sarantos, M., R.M. Killen, W.E. McClintock, E.T. Bradley, R.J. Vervack, M. Benna, and J.A.
735 Slavin, Limits to Mercury's magnesium exosphere from MESSENGER second flyby
736 observations, Planet. Space Sci., 59, 1992-2003, (2011)

737 Solomon S.C., and B.J. Anderson, The MESSENGER Mission : Science and Implementation
738 Overview, ed. by S. Solomon, L. Nittler, B. Anderson. Cambridge Planetary Science,
739 (Cambridge University Press, Cambridge 2018), 1-29

740 Stern, A., The lunar atmosphere : history, status, current problems, and context, Rev. Geophys.,
741 37, 453-491, (1999)

742 Weider, S.Z, L.R. Nittler, R.D. Starr, E.J. Crapster-Pregont, P.N. Peplowski, N.W. Denevi,
743 J.W. Head, P.K. Byrne, S.A. Hauk II, D.S. Ebel, and S.C. Solomon, Evidence for
744 geochemical terranes on Mercury : global mapping of major elements with
745 MESSENGER's X-ray spectrometer, Earth Planet. Sci. Lett., 416, 109-120, (201